EARTH'S INTERIOR

Dehydration melting at the top of the lower mantle

Brandon Schmandt,[1]* Steven D. Jacobsen,[2]* Thorsten W. Becker,[3]
Zhenxian Liu,[4] Kenneth G. Dueker[5]

The high water storage capacity of minerals in Earth's mantle transition zone (410- to 660-kilometer depth) implies the possibility of a deep H_2O reservoir, which could cause dehydration melting of vertically flowing mantle. We examined the effects of downwelling from the transition zone into the lower mantle with high-pressure laboratory experiments, numerical modeling, and seismic *P*-to-*S* conversions recorded by a dense seismic array in North America. In experiments, the transition of hydrous ringwoodite to perovskite and (Mg,Fe)O produces intergranular melt. Detections of abrupt decreases in seismic velocity where downwelling mantle is inferred are consistent with partial melt below 660 kilometers. These results suggest hydration of a large region of the transition zone and that dehydration melting may act to trap H_2O in the transition zone.

The water content of the upper mantle as sampled by mid-ocean ridge basalts is 0.005 to 0.02 weight % (wt %) (*1*), but a potentially much larger, deep reservoir of water may exist in the mantle transition zone between 410- and 660-km depth owing to the 1 to 3 wt % H_2O storage capacity of the major mineral phases wadsleyite and ringwoodite (*2*, *3*). Convective mass transfer across the boundaries of the transition zone could cause dehydration melting, and consequently filtering of incompatible elements, if water contents in the transition zone exceed that of the shallower or deeper mantle (*4*). An open question is whether transition zone water contents are sufficient to cause dehydration melting where there is downward flow into the lower mantle.

Dehydration melting due to downward flow across the 660-km discontinuity (660) would require both hydration of ringwoodite in the transition zone and low water storage capacity at the top of the lower mantle. The recent discovery of a ~1.5 wt % H_2O hydrous ringwoodite inclusion in a diamond (*5*) demonstrates that, at least locally, the mantle transition zone may be close to water saturation. Regional detections of high seismic attenuation (*6*) and electrical conductivity (*7*) in the transition zone suggest hydration at larger scales. However, high-pressure experiments on the incorporation of H_2O into silicate perovskite vary widely from 0.0001 wt % (*8*) to 0.4 wt % H_2O (*9*), with other estimates in between (*10*). Recent experiments on coexisting phase assemblages indicate a high H_2O partition coefficient between ringwoodite and silicate perovskite of 15:1 (*11*), suggesting a large contrast in water storage capacity at the boundary between the base of the transition zone and the top of the lower mantle.

We integrated laboratory experiments, seismic imaging, and numerical models of mantle flow to investigate mass transfer and melting at the interface between the transition zone and lower mantle beneath North America (*12*). We conducted in situ

---

[1]Department of Earth and Planetary Science, University of New Mexico, Albuquerque, NM, USA. [2]Department of Earth and Planetary Sciences, Northwestern University, Evanston, IL, USA. [3]Department of Earth Sciences, University of Southern California, Los Angeles, CA, USA. [4]Geophysical Laboratory, Carnegie Institution of Washington, Washington DC, USA. [5]Department of Geology and Geophysics, University of Wyoming, Laramie, WY, USA.
***Corresponding author. E-mail: bschmandt@unm.edu (B.S.); steven@earth.northwestern.edu (S.D.J.)**

laser heating experiments to directly transform hydrous ringwoodite to form silicate perovskite and (Mg,Fe)O in a diamond-anvil cell (DAC) and analyzed the recovered sample with synchrotron–Fourier transform infrared (FTIR) spectroscopy and transmission electron microscopy (TEM) (Fig. 1). FTIR spectra taken away from the laser-heated spots are typical for hydrous Fe–bearing ringwoodite (*13*). Within the laser-heated spots where perovskite and (Mg,Fe)O formed, there is still strong absorption in the OH-stretching region, although notably different from absorption that occurred before heating (Fig. 1B). Within laser-heated spots, the maximum in OH-stretching absorbance occurs at ~3400 cm^{-1}, and there is a sharp peak at ~3680 cm^{-1} associated with brucite (*8*). Both features are common to the spectra of previous studies (*9*, *10*) that reported 0.1 to 0.4 wt % H_2O in perovskite. Recovery of the sample from the DAC allowed detailed study by TEM (Fig. 1C), which shows that nanoscale, intergranular silicate melt was formed around single crystals of perovskite. The broad, asymmetric absorption band observed in Fig. 1B thus likely represents OH in the melt phase, because the partition coefficient of H_2O between ringwoodite and silicate perovskite is about 15:1 (*11*).

Partial melt in the mantle strongly affects seismic velocities and can create sharp velocity gradients where it is adjacent to subsolidus mantle. If dehydration melting occurs where ringwoodite is entrained downward across the 660, then in situ detection would be feasible in areas with dense seismic sampling. A major component of the EarthScope project (*14*) is the deployment of broadband seismometers with ~70-km spacing across the United States (Fig. 2A). These data enable imaging of geographic variations in seismic structure near the 660. We isolated conversions of earthquake seismic waves from *P*-to-*S* (*Ps*) as a result of sharp vertical gradients in seismic velocity with receiver function analysis (*15*). *Ps* receiver functions were then mapped to depth using *P* and *S* tomography models, creating a high-fidelity, common conversion point (CCP) image of vertical velocity gradients near

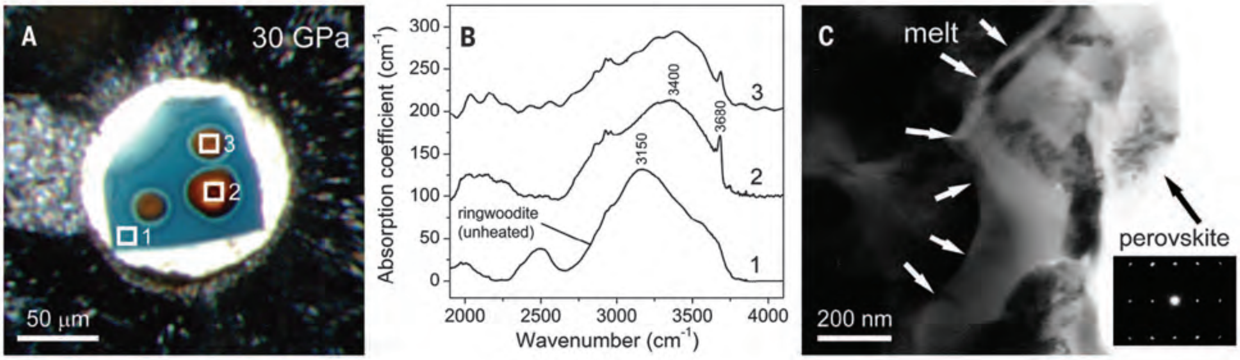

Fig. 1. Laboratory experiments on hydrous ringwoodite. (**A**) Single-crystal of hydrous ringwoodite (blue crystal) containing 1 wt % H_2O inside a DAC at 30 GPa. The sample was laser heated to 1600°C in several spots (orange circles) to perform direct transformation to perovskite and (Mg,Fe)O. (**B**) Synchrotron-FTIR spectra of the recovered sample in three locations: an unheated part of the crystal (spectrum 1) and two locations within laser-heated spots (spectra 2 and 3). FTIR spectra were collected with a 10 μm by 10 μm aperture, illustrated and numbered by white boxes in (A). (**C**) TEM within a laser-heated spot (position 2) shows crystals of perovskite and intergranular amorphous quench (melt).

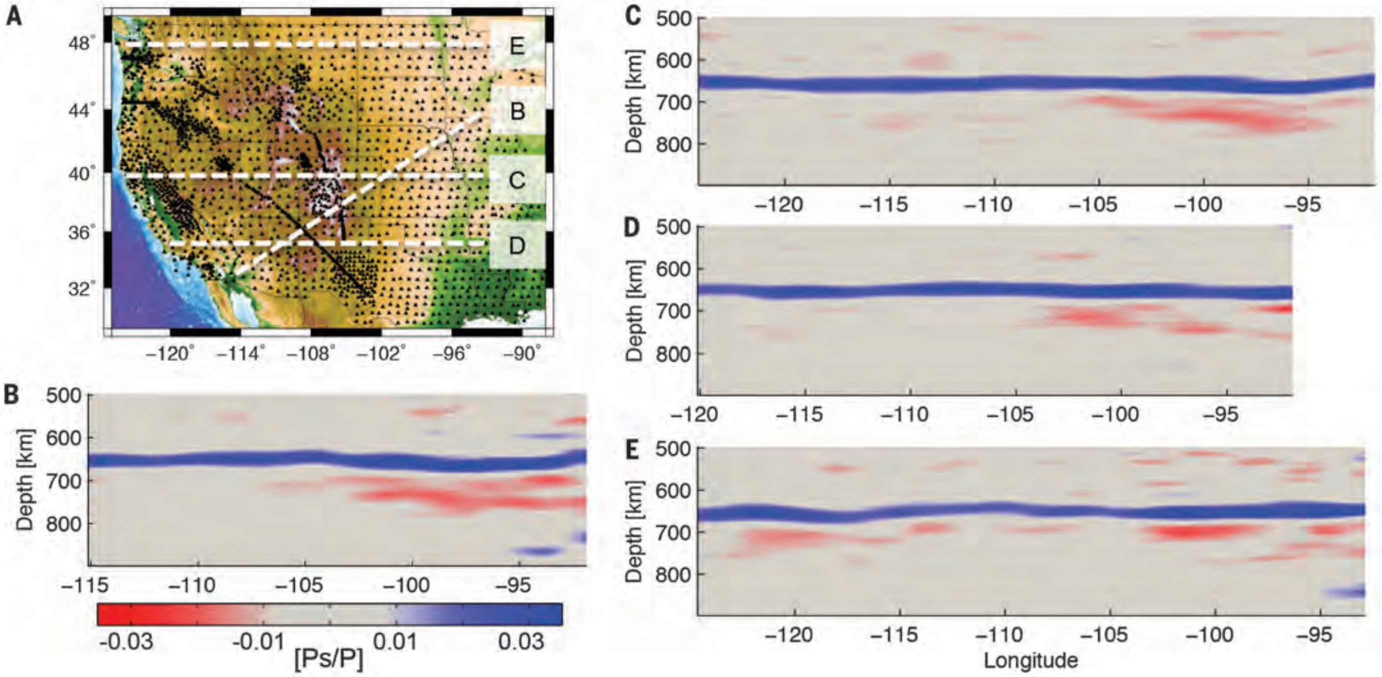

Fig. 2. Vertical cross-sections through the CCP image. (**A**) Map of the study region with broadband seismometers denoted by black triangles and the locations of vertical cross-sections shown in (B) to (E) denoted by white dashed lines. (**B**) Vertical cross-section through the CCP image. The location of the eastern end of the cross-section is shown as B′ in (A). The 660, which separates the transition zone and lower mantle, is clearly imaged by 2.5 to 4% amplitude positive *Ps/P* arrivals in all cross-sections. Negative arrivals beneath the 660 have amplitudes ≤2.2%. (**C** to **E**) Vertical cross-sections through the CCP image beneath the three other lines labeled in (A).

the 660 beneath much of the continental United States (*12*, *16*).

Positive-amplitude *Ps* conversions clearly define the abrupt velocity increase with depth at the 660 beneath the entire array (Fig. 2), and other, weaker discontinuities are sporadically detected in the mantle beneath the EarthScope array (*16*, *17*). Common secondary features in the CCP image near the 660 are negative-amplitude *Ps* conversions in the uppermost 120 km of the lower mantle. A map of the locations of sub-660 negative *Ps* conversions with magnitude >1.25% of the direct *P*-wave shows that these features are prevalent beneath a large area including the Great Plains and near the northern margin of the array (Figs. 2 and 3). In contrast, negative *Ps* conversions near the top of the lower mantle are absent beneath the southwestern United States. The amplitude of the negative *Ps* conversions from beneath the 660 is up to 2.2% of the direct *P*-wave amplitude. For a negative *Ps* conversion near the top of the lower mantle, 730 km, an amplitude of 2% is consistent with a decrease in shear velocity of 2.6% over a depth interval of ≤20 km based on a synthetic calculation of receiver functions (*12*). The areas where negative *Ps* conversions are detected are not correlated with volumes of anomalously low-velocity mantle in tomography images (*16*, *18*); hence, a thermal origin for the reduced velocities is unlikely.

To assess the correlation between the locations of abrupt velocity decreases near the top of the lower mantle and convective flow patterns, we used numerical models of mantle circulation. Computations were solved for flow using radially varying viscosity and prescribed plate motions at the surface (*12*, *19*). Regional mantle flow rates are controlled by the poorly constrained ratio between density anomalies and viscosity, but flow directions are mainly determined by density anomaly patterns. To explore this sensitivity, we used multiple tomography models (*15*, *17*, *19*) to infer density fields. For length scales less than ~500 km, the resulting vertical flow patterns at 660-km depth vary widely between models, but circulation models yield a common long-wavelength pattern of vertical flow across the 660 (Fig. 3). Downward flow through the 660 is dominant beneath the Great Plains and along the U.S.-Canada border, and upward flow is dominant beneath the southwestern United States (Fig. 3). This pattern is driven by large volumes of anomalously high-velocity lower mantle, which are inferred to be subducted slabs sinking beneath central and eastern North America (*20*–*22*).

Comparing the results of two flow models shows that nearly all the locations of negative *Ps* conversions beneath the 660 coincide with downward flow (Fig. 3). One flow model is based on an inversion of travel-time data from the EarthScope stations using the TX-2008 global tomography model (*20*) as a starting model (Fig. 3A, SH11-TX). The other flow model is based on density structure from the global tomography model S40RTS (*18*), which does not include EarthScope seismic data and hence only recovers long-wavelength structure (Fig. 3B). Consequently, the first flow model includes stronger short-wavelength variations (*19*), but the long-wavelength pattern is consistent. Comparing the distributions of vertical velocities across the 660 in the entire CCP image and the subset of the CCP image where sub-660 negative *Ps* conversions are detected demonstrates that the latter area is biased toward regions of downward flow (Fig. 4). For both flow models, less than 3% of sub-660 negative *Ps* conversions are found in areas with upward flow across the 660. Comparisons with smooth three-dimensional velocity structure at 660-km depth, rather than vertical flow velocity, show some bias toward higher tomographically imaged shear velocities in areas with sub-660 negative *Ps* conversions, but less similarity between the two models than is observed for the comparison with vertical flow.

The correlation between abrupt seismic velocity decreases near the top of the lower mantle and

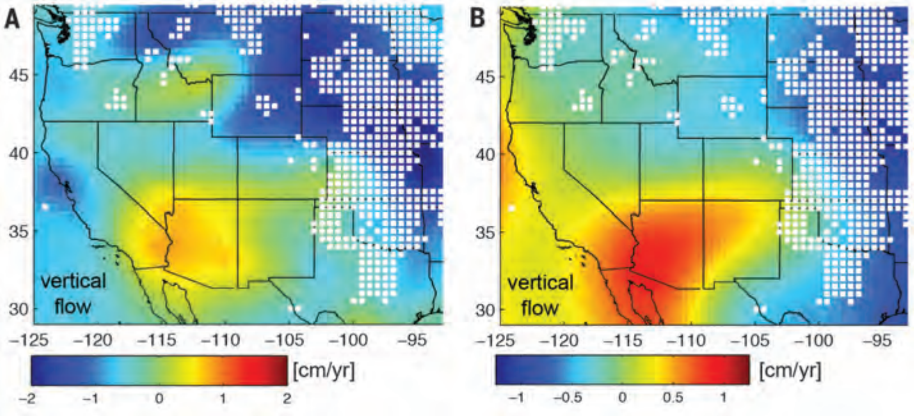

Fig. 3. Vertical flow between the transition zone and lower mantle. (**A**) The background color shows the vertical flow velocity at the boundary between the transition zone and lower mantle predicted by a mantle circulation model using density structure inferred from the SH11-TX tomography model. White squares denote locations where the seismic CCP image detects velocity decreases with depth in the depth range of 670 to 800 km. (**B**) The background color shows the vertical flow velocity predicted using the S40RTS tomography model. In both models, velocity decreases near the top of the lower mantle are absent beneath the southwestern United States where upward flow is predicted and prevalent in areas where downward flow into the lower mantle is predicted.

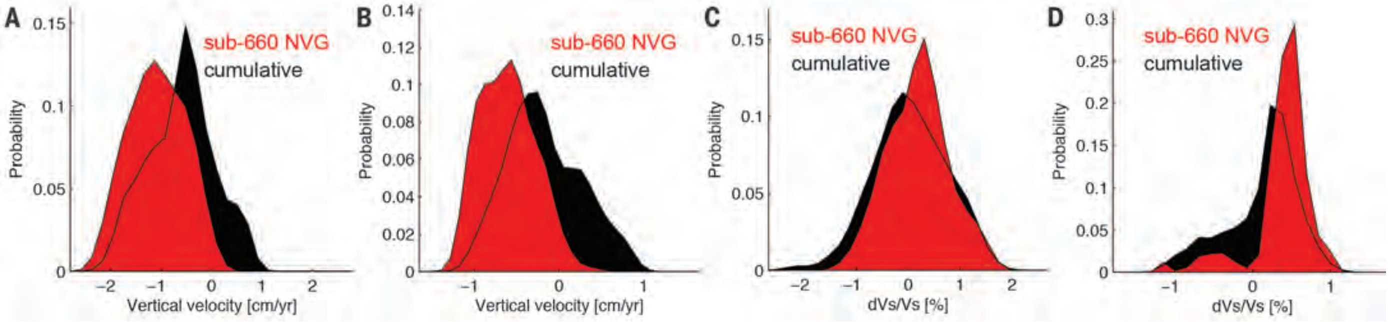

Fig. 4. Distributions of vertical flow and seismic velocity variations at 660 km. (**A**) Probability density functions (PDFs) of vertical flow velocity at 660-km depth from the convection model using SH11-TX tomography. The PDF in red represents the subset of the CCP image where negative velocity gradients are detected beneath the 660 (sub-660 NVG), and the PDF in black represents the cumulative area from the CCP image. The cumulative area of the CCP image includes the area within 200 km of the seismometers shown in Fig. 2A. (**B**) PDFs of vertical flow velocity from the convection model using S40RTS tomography. (**C**) PDFs of mantle shear velocity variations near the 660 from the tomography model SH11-TX. (**D**) PDFs of mantle shear velocity variations from the tomography model S40RTS.

areas of downwelling across the 660 is consistent with the occurrence of dehydration melting as observed in our laboratory experiments. An alternative bulk-compositional origin of low velocities near the top of the lower mantle is segregated basalt that may be neutrally buoyant (*23*) and would reduce seismic velocities (*24*).

However, long-term accumulation of basalt near the top of the lower mantle is not expected to be preferentially present where there is downwelling across the 660 and absent where there is not. The areas of downward flow across 660 do not all coincide with local presence of subducted slabs, so a direct link to composition of the sinking Farallon slab cannot explain the negative velocity gradients below 660. Assuming that the velocity reductions result from partial melt, and that the shear-velocity decrease per percent of melt is between 2.6 and 3.8%, as predicted for partial melt near 400-km depth (*25*), then 0.68 to 1% melt could explain a 2.6% shear velocity reduction indicated by negative *Ps* conversions with amplitude of 2% in the CCP image.

Prediction of partial melt percentages at 660-km depth for various H_2O contents requires knowledge of water partition coefficients between minerals and melts at relevant pressure-temperature (*P-T*) conditions in the peridotite-saturated compositional system. At present, experiments in the hydrous peridotite system at conditions near the 660 have not been performed. However, using experimental results for partial melting near the 410-km discontinuity (410) in a bulk peridotite system with 1 wt % H_2O indicates that ~5% partial melt at 410 km is expected (*26*, *27*) where the partition coefficient of H_2O between wadsleyite and olivine is at least 5:1 (*11*). We can expect at least 5% partial melt in a bulk 1 wt % H_2O peridotite system where the partition coefficient between ringwoodite and silicate perovskite is 15:1 (*11*). Thus, production of up to 1% melt by dehydration melting of hydrous ringwoodite viscously entrained into the lower mantle is feasible.

The density of hydrous melt near the top of the lower mantle is uncertain, but it is likely buoyant with respect to the top of the lower mantle (*28*). Hence, we expect that the velocity decreases imaged beneath the 660 are transient features resulting from ongoing downward flow through the 660 that is driven by sinking slabs in the lower mantle. Eventually, the slightly buoyant hydrous melt would percolate upward, returning H_2O to the transition zone (*4*). Dehydration melting has also been suggested to occur where hydrous wadsleyite upwells across the 410 and into the olivine stability field (*3*, *27*). Experiments indicate that hydrous melt is gravitationally stable atop the 410 (*28*), so once melt is generated, it may remain or spread laterally rather than maintaining a clear correlation with ongoing vertical flow patterns. Seismic detections of a low-velocity layer atop the 410 are common but laterally sporadic beneath North America and globally (*29*, *30*). The combination of dehydration melting driven by downwelling across the 660 and upwelling across the 410 could create a long-term H_2O trap in the transition zone (*4*).

REFERENCES AND NOTES

1. A. E. Saal, E. H. Hauri, C. H. Langmuir, M. R. Perfit, *Nature* **419**, 451–455 (2002).
2. J. R. Smyth, *Am. Mineral.* **72**, 1051 (1987).
3. D. L. Kohlstedt, H. Keppler, D. C. Rubie, *Contrib. Mineral. Petrol.* **123**, 345–357 (1996).
4. D. Bercovici, S. Karato, *Nature* **425**, 39–44 (2003).
5. D. G. Pearson *et al.*, *Nature* **507**, 221–224 (2014).
6. H. Zhu, E. Bozdag, T. S. Duffy, J. Tromp, *Earth Planet. Sci. Lett.* **381**, 1–11 (2013).
7. A. Kelbert, A. Schultz, G. Egbert, *Nature* **460**, 1003–1006 (2009).
8. N. Bolfan-Casanova, H. Keppler, D. C. Rubie, *Geophys. Res. Lett.* **30**, 1905 (2003).
9. M. Murakami, K. Hirose, H. Yurimoto, S. Nakashima, N. Takafuji, *Science* **295**, 1885–1887 (2002).
10. K. Litasov *et al.*, *Earth Planet. Sci. Lett.* **211**, 189–203 (2003).
11. T. Inoue, T. Wada, R. Sasaki, H. Yurimoto, *Phys. Earth Planet. Inter.* **183**, 245–251 (2010).
12. Materials and methods are available on *Science* Online.
13. S. D. Jacobsen, J. R. Smyth, H. A. Spetzler, C. M. Holl, D. J. Frost, *Phys. Earth Planet. Inter.* **143-144**, 47–56 (2004).
14. R. A. Kerr, *Science* **340**, 1283–1285 (2013).
15. J. P. Mercier, M. G. Bostock, A. M. Baig, *Geophysics* **71**, SI95–SI102 (2006).
16. B. Schmandt, K. G. Dueker, E. D. Humphreys, S. M. Hansen, *Earth Planet. Sci. Lett.* **331-332**, 224–236 (2012).
17. B. Tauzin, R. D. van der Hilst, G. Wittlinger, Y. Ricard, *J. Geophys. Res. Solid Earth* **118**, 2307–2322 (2013).
18. J. Ritsema, A. Deuss, H. J. van Heijst, J. H. Woodhouse, *Geophys. J. Int.* **184**, 1223–1236 (2011).
19. T. W. Becker, C. Faccenna, E. D. Humphreys, A. R. Lowry, M. S. Miller, *Earth Planet. Sci. Lett.* (2014).
20. N. A. Simmons, A. M. Forte, S. P. Grand, *Geophys. J. Int.* **177**, 1284–1304 (2009).
21. B. Steinberger, *Phys. Earth Planet. Inter.* **118**, 241–257 (2000).
22. A. M. Forte, R. Moucha, N. A. Simmons, S. P. Grand, J. X. Mitrovica, *Tectonophysics* **481**, 3–15 (2010).
23. C. T. A. Lee, W. P. Chen, *Earth Planet. Sci. Lett.* **255**, 357–366 (2007).
24. W. B. Xu, C. Lithgow-Bertelloni, L. Stixrude, J. Ritsema, *Earth Planet. Sci. Lett.* **275**, 70–79 (2008).
25. S. Hier-Majumder, A. Courtier, *Earth Planet. Sci. Lett.* **308**, 334–342 (2011).
26. M. M. Hirschmann, T. Tenner, C. Aubaud, A. C. Withers, *Phys. Earth Planet. Inter.* **176**, 54–68 (2009).
27. T. J. Tenner, M. M. Hirschmann, A. C. Withers, P. Ardia, *Contrib. Mineral. Petrol.* **163**, 297–316 (2012).
28. T. Sakamaki, A. Suzuki, E. Ohtani, *Nature* **439**, 192–194 (2006).
29. B. Schmandt, K. G. Dueker, S. M. Hansen, J. J. Jasbinsek, Z. Zhang, *Geochem. Geophys. Geosyst.* **12**, Q08014 (2011).
30. B. Tauzin, E. Debayle, G. Wittlinger, *Nat. Geosci.* **3**, 718–721 (2010).

ACKNOWLEDGMENTS

Seismic data were acquired from the IRIS Data Management Center. This work was supported by NSF grants EAR-0748707 to S.D.J. and EAR-1215720 to T.W.B., and by the David and Lucile Packard Foundation and Carnegie/DOE Alliance Center (CDAC) to S.D.J. Portions of this work were performed at GSECARS (Sector 13), Advanced Photon Source (APS), Argonne National Laboratory. GSECARS is supported by the NSF (EAR-1128799) and U.S. Department of Energy (DOE) (DE-FG02-94ER14466). Use of the APS was supported by the DOE-BES (Basic Energy Sciences) (DE-AC02-06CH11357). Portions of this work were performed at beamline U2A of the National Synchrotron Light Source (NSLS), Brookhaven National Laboratory. U2A is supported by COMPRES (Consortium for Materials Properties Research in Earth Sciences) under NSF Cooperative Agreement EAR 11-57758 and DOE-NNSA (National Nuclear Security Administration) (DE-FC-52-08NA28554, CDAC). Use of the NSLS was supported by the DOE-BES (DE-AC02-98CH10886). We thank S. Demouchy, D. J. Frost, E. H. Hauri, M. M. Hirschmann, F. Langenhorst, J. F. Lin, G. Shen, V. B. Prakapenka, and J. R. Smyth for discussions and help with experiments. B.S. and S.D.J. designed the research and wrote the paper. B.S. conducted the seismological research, and S.D.J. performed the experiments. T.W.B. produced the mantle circulation models, Z.L. contributed to the FTIR experiments, and K.G.D. contributed to seismic imaging. All authors participated in data interpretation and contributed to the manuscript.

SUPPLEMENTARY MATERIALS

www.sciencemag.org/content/344/6189/1265/suppl/DC1
Materials and Methods
Figs. S1 to S4
References (*31*–*38*)
Additional Data Tables S1 to S3

13 March 2014; accepted 12 May 2014
10.1126/science.1253358